Frequency-locked Wireless Multifunctional Surface Acoustic Wave Sensors

Luyu Bo[†], *Jiali Li*[†], *Zhide Wang*, *Chongpeng Qiu*, *Bowen Cai*,
Yingshan Du, *Teng Li*, *Hongye Liu*, *Zhenhua Tian**

Luyu Bo, Jiali Li, Zhide Wang, Chongpeng Qiu, Bowen Cai, Teng Li, Hongye Liu,
Prof. Zhenhua Tian
Department of Mechanical Engineering,
Virginia Polytechnic Institute and State University, Blacksburg, VA, 24060, USA
E-mail: tianz@vt.edu (Z.T.)

Yingshan Du
Department of Biomedical Engineering and Sciences,
Virginia Polytechnic Institute and State University, Blacksburg, VA, 24060, USA

[†] L.B. and J.L. contributed equally to this work.
[*] Correspondence to: tianz@vt.edu (Z.T.)

Keywords: Surface acoustic wave sensors, wireless strain and temperature sensing, wireless vibration sensing, water presence detection, laser Doppler vibrometry

Abstract

Surface acoustic waves (SAWs) have shown great potential for developing sensors for structural health monitoring (SHM) and lab-on-a-chip (LOC) applications. Existing SAW sensors mainly rely on measuring the frequency shifts of high-frequency (*e.g.*, >0.1 GHz) resonance peaks. This study presents frequency-locked wireless multifunctional SAW sensors that enable multiple wireless sensing functions, including strain sensing, temperature measurement, water presence detection, and vibration sensing. Our sensors leverage SAW resonators on piezoelectric chips, inductive coupling-based wireless power transmission, and, particularly, a frequency-locked wireless sensing mechanism that works at low frequencies (*e.g.*, <0.1 GHz). This mechanism locks the input frequency on the slope of a sensor's reflection spectrum and monitors the reflection signal's amplitude change induced by the changes of sensing parameters. The proof-of-concept experiments show that our wireless sensors can operate in a low-power active mode for on-demand wireless strain measurement, temperature sensing, and water presence detection. Moreover, our sensors can operate in a power-free passive mode for vibration sensing, with results that agree well with laser vibrometer measurements. We anticipate that the designs and mechanisms of our frequency-locked wireless SAW sensors will inspire researchers to develop future wireless multifunctional sensors for SHM and LOC applications.

1. Introduction

Surface acoustic waves (SAWs) propagating on piezoelectric chips[1-3] have been attracting increasing interest for the development of physical,[4-9] chemical,[10-13] and biological[14-17] sensors for structural health monitoring (SHM),[18-21] gas composition monitoring,[22-28] and lab-on-a-chip (LOC) applications.[29-31] These SAW sensors have microfabricated interdigital transducers (IDTs) on piezoelectric substrates (*e.g.*, quartz, $LiNbO_3$, $LiTaO_3$, ZnO, AlN, *etc.*) to generate and acquire SAWs of different modes, such as the commonly used Rayleigh mode, the low attenuation shear horizontal mode, and the Love mode guided by the interface of a piezoelectric substrate and a thin top layer.[3, 20] With IDTs arranged in different configurations, such as a delay line configuration with a pair of IDTs in a pitch-catch arrangement and a resonator configuration with an IDT surrounded by Bragg reflectors, various SAW sensors have been developed to measure and monitor physical parameters (*e.g.*, temperature,[32-36] strain,[4-6] humidity,[37-42] magnetic field,[9, 43] *etc.*), concentrations of chemicals (*e.g.*, H_2, H_2S, NO_2, NH_3, *etc.*),[22-28] and concentrations of bioparticles (*e.g.*, bacteria, viruses, DNA, and proteins)[14-17] based on different sensing mechanisms. For example, relying on the mechanism that temperature increase leads to sensor thermal expansion and SAW velocity change, SAW temperature sensors have been developed.[32-36] Leveraging the mass-loading effect on resonance frequency shifts,[15-17] chemical and biological sensors have been developed. To increase the sensitivity and specificity, these sensors usually have sensing layers that specific targets of interest can bond to, such as Au layers with immobilized probe DNA and antibodies.[15-17]

To develop wireless sensors for embeddable and implantable scenarios, Internet of Things (IoT), and SHM, wireless power transmission (WPT) technologies based on electromagnetic and ultrasonic waves have received great attention.[44-46] By integrating WPT modules with SAW sensors, various wireless SAW sensors have been developed for different applications such as magnetic field monitoring,[47] heart rate and blood pressure measurements,[48-49] and sensing of gas, temperature, strain, *etc*.[50-59] For example, Yang *et al*. developed wireless SAW sensors integrated with an antenna and a Co_{40}-Fe_{40}-B_{20} magnetic sensitive layer for monitoring magnetic field changes.[47] Zou *et al*. demonstrated implantable wireless SAW sensors for measuring pulse pressures and heart rates.[48] Devkota *et al*. presented a wireless SAW sensor with a metal-organic framework sensing layer for monitoring CO_2 and CH_4.[50] Kim *et al*. manufactured wireless SAW sensors with magnetic antennas for monitoring underground temperatures.[51] Given the success of these wireless SAW sensors, they mainly rely on tracking the SAW resonance frequency shift Δf_R,[47-51] which needs to perform a high-resolution frequency scanning to obtain a frequency response curve (*e.g.*, *S*-parameter or impedance curve) and quickly identify the resonance frequency. To increase the sensitivity, *i.e.*, increasing the frequency shift Δf_R induced by the sensing parameter change, those wireless SAW sensors usually need to push the SAW resonance frequency to the 100s of MHz to 10s of GHz range by greatly reducing the IDT's electrode width and spacing. This increases the challenges in SAW sensor fabrication and imposes the demand for high-end equipment that can precisely track the changes of high-frequency resonance peaks.

This study presents frequency-locked wireless multifunctional SAW sensors that offer multiple wireless sensing functions, including strain sensing, temperature measurement, water presence detection, and passive vibration sensing. The wireless SAW sensors are composed of single IDT-based SAW resonators on piezoelectric chips and inductive coupling-based WPT antennas with matching circuits. They leverage a frequency-locked wireless sensing mechanism, rather than the mechanism of precisely tracking resonance frequency shifts used by most wireless SAW sensors.[47-58] The mechanism of our wireless SAW sensor uses an input frequency locked on the slope of the sensor's reflection spectrum and monitors the reflection signal's amplitude changes induced by the changes of sensing parameters, such as strain changes, temperature variations, and water presence. Through proof-of-concept experiments, we have shown that our wireless SAW sensors can operate in a low-power active mode for on-demand wireless strain measurement, temperature monitoring, and water presence detection. Moreover, our sensors have been demonstrated to operate in a power-free passive mode for real-time vibration sensing, and the vibration waveforms and frequency spectra measured by our sensors agree well with the data acquired by a laser Doppler vibrometer. Compared to most wireless SAW sensors tracking frequency shifts,[47-58] our wireless SAW sensors with the frequency-locked wireless sensing mechanism don't need to perform high-resolution scanning at many frequencies to precisely track the frequency shift, thus potentially saving acquisition time and enabling quick response. Additionally, our wireless sensing mechanism is applicable for low-frequency (<0.1 GHz) SAW resonators; in contrast, the wireless SAW sensors that track resonance frequency shifts typically work in a higher frequency range (>0.1 GHz).[47-58] The usage of low-frequency SAW resonators lessens the demand for high-end, high-sampling-rate data acquisition equipment and the challenge in SAW sensor manufacturing. With these features and multiple wireless sensing functions, we anticipate that the sensor designs and sensing mechanisms presented in this work will inspire researchers to develop future wireless physical, chemical, and biological sensors.

2. Results and Discussion

2.1. Design and mechanism of wireless SAW sensors

Our wireless SAW sensing approach (see **Figure 1a** for a schematic) leverages three key modules, including (i) a SAW chip with an IDT deposited on a $LiNbO_3$ piezoelectric wafer to generate SAWs for enabling multifunctional sensing of strain, temperature, water presence, and vibration, (ii) a customized WPT module for wirelessly sending power from the WPT transmitter to the receiver, as well as returning sensing signals from the receiver to the transmitter, and (iii) matching circuits to adjust the resonance frequencies of the WPT transmitter and receiver to match the SAW resonance frequency. As illustrated by a setup schematic in **Figure 1b** for performing wireless sensing (also see **Figure S1** for an equivalent circuit diagram), a function generator is used to generate a continuous input signal denoted as $s_t(t)=A_te^{i\omega t}$ where t, ω, and A_t are time, angular frequency, and input amplitude, respectively. As indicated by the blue arrows in **Figure 1b**, the input signal is sent to the WPT transmitting coil, and through inductive coupling[60-62] the input signal's energy is wirelessly transmitted to the WPT receiving coil and then to the SAW chip. The energy reflected by the SAW chip returns to the WPT transmitter, as indicated by the brown arrows in **Figure 1b**. The return signal is denoted as $s_r(t)=A_re^{i(\omega t+\Delta\varphi)}$ where A_r and $\Delta\varphi$ are amplitude and phase shift. An oscilloscope is used to monitor the summation (denoted as $s_m = s_r + s_t$) of input and return signals.

The mechanism of our frequency-locked wireless SAW sensing approach is illustrated in **Figure 1c.** Different from the commonly used mechanism that measures frequency shifts through high-resolution frequency scanning,[47-51] our mechanism monitors signal amplitude changes at a locked frequency. For example, a function generator provides a continuous input signal at a frequency locked at the center of the S_{11}-frequency curve's falling slope (illustrated in **Figure 1c**). When the SAW sensor is subjected to loads and environmental condition changes, the sensor's S_{11}-frequency curve experiences frequency shifts and/or value changes. Accordingly, the reflected signal s_r at the locked frequency varies, and the total signal $s_m = s_t + s_r$ measured by an oscilloscope in the sensing setup (**Figure 1b**) becomes different. The relation between the S_{11} value and the measurement signal s_m is mathematically described in Section S1 of the Supporting Information, in order to better understand the sensing mechanism. By monitoring the total signal's amplitude change, our approach is able to detect changes in environmental conditions and loads applied on the sensor, further enabling on-demand strain sensing, temperature sensing, and water presence detection as illustrated in **Figure 1d** to **1f**. Moreover, as the piezoelectric substrate of the sensor can convert mechanical energy to electrical energy,[63] our wireless sensor can be operated in an input power-free, passive vibration sensing mode. When the piezoelectric substrate is subjected to vibration, a dynamic electric potential is generated between the IDT's two groups of electrodes, and the signal can be wirelessly returned to the WPT transmitting coil and then measured by an oscilloscope.

A compression load on the SAW sensor in the direction perpendicular to the IDT electrode reduces the electrode period, thus increasing the SAW resonance frequency and shifting the S_{11} curve to the right (illustrated by a purple curve in **Figure 1c**). When the SAW sensor is subjected to a temperature increase, the thermal expansion increases the IDT electrode period (see **Figure 1e**), thus reducing the resonance frequency and shifting the S_{11} curving to the left side (brown curve in **Figure 1c**). After submerging the SAW sensor in water (see **Figure 1f**), the SAW energy leaks into the water, leading to an S_{11}-frequency curve with higher S_{11} values (blue curve in **Figure 1c**) than the original case (black curve in **Figure 1c**). Because of the S_{11} curve changes (*e.g.*, frequency shifts and/or value changes), the S_{11} value at the locked test frequency changes, leading to reflection signal amplitude variations. Compared to previous SAW sensors that mainly use frequency shifts for sensing, the frequency-locked sensing method doesn't need to perform a high-resolution scanning at many frequencies to obtain the frequency shift, thus saving data acquisition time and enabling quick response. Moreover, our method reduces the requirement of using an expensive, high-performance network analyzer for measuring the frequency response curve in real-time. In addition, our sensing mechanism is applicable for low-frequency (<0.1 GHz) SAW resonators, while the resonance frequency shift-based approach typically uses SAW resonators working in a higher frequency range, *e.g.*, 0.1 to 10 GHz.[47-58] The usage of low-frequency SAW resonators lessens the demand for high-end, high-sampling-rate measurement equipment. It also reduces the challenge in SAW sensor fabrication, as higher frequency SAW resonators have smaller electrode widths and spacings.

Based on the sensing mechanism illustrated in **Figure 1**, we have designed and fabricated wireless SAW sensors. **Figure S2** shows a microscopic image of a cleanroom fabricated IDT and a fully integrated wireless SAW sensor with an IDT chip, a matching circuit, and a WPT coil. After sensor fabrication, we characterized the fabricated SAW sensors by measuring their S_{11}-frequency curves. Moreover, we performed a series of proof-of-concept experiments to demonstrate our wireless sensor's functions including active-mode, on-demand strain sensing, temperature sensing, and water presence detection, as well as passive-mode, real-time vibration sensing. The results of characterization and proof-of-concept experiments, as well as their related data analysis are given below.

2.2. Optimization and characterization of wireless SAW sensors

Figure 2a shows an equivalent circuit diagram of the wireless SAW sensing approach. The energy transmitting side (**Figure 2a** left), connected to an alternating current (AC) power source (*e.g.*, a function generator), has a matching circuit with a capacitance C_T, as well as a WPT transmitting coil with an inductance L_T and a resistance R_T. The SAW sensing side (**Figure 2a** right) has an IDT connected to a matching circuit with a capacitance C_R and then a coil-based WPT receiver with an inductance L_R and a resistance R_R. Our approach leverages inductive coupling[60] to transfer energy/information between the transmitting and receiving coils. To maximize the wireless SAW sensor's energy efficiency, we optimized the parameters of WPT coils and matching circuits to let the peak energy transfer frequency match the SAW resonance frequency. Three-dimensional (3D) finite element simulations were performed to optimize the design parameters including capacitances of matching circuits, as well as transmitting and receiving coil diameters and numbers of turns. The 3D simulation model (see **Figure S3**) includes a WPT transmitting coil with a matching circuit, a WPT receiving coil with its matching circuit, a domain with air surrounding the circuits, as well as a thin layer outside the simulation domain for minimizing boundary reflections. **Figure 2b** shows simulated magnetic intensity (color) and flux (arrow) fields in the *x-z* plane, revealing a strong magnetic field induced in a region surrounding the receiving coil when using optimized circuit parameters. Details of the WPT module's design and parameters are provided in the Experimental Section.

Following the optimization and fabrication of a wireless SAW sensor, we characterized the sensor by measuring its S_{11}-frequency curves for cases with different distances between the parallelly arranged transmitting and receiving coils. The experimental results (**Figure 2c**) show that the S_{11} value gradually changes in a range of -0.71 to -20.78 dB in a test frequency range of 36 to 42 MHz when the coil-to-coil distance is 15 mm. This curve also shows a valley at 39 MHz matching the SAW resonance frequency. When the coil-to-coil distance increases to 40 mm, the S_{11} range narrows down to -0.68 to -8.45 dB. As the WPT module uses inductive coupling, typically for near-field applications, the coil-to-coil distance is on the centimeter scale. This distance can be increased by increasing the inductive coil diameters.

At the SAW sensor's resonance frequency of 39 MHz, the comparison in **Figure 2d** shows that the S_{11} value gradually increases with the coil-to-coil distance increase. The S_{11} value indicates the ratio of the power reflected back to port 1 to the power output from port 1. Hence, S_{11} depends on the entire load, *i.e.*, the combination of all the components on the right side of the power source in the circuit diagram in **Figure 2a**. With the coil-to-coil distance increase, the increase of S_{11} indicates more energy reflected back to port 1 and less energy consumed by the entire load including both the WPT module and the SAW sensor. After characterization, the fabricated sensors are further validated through wireless strain sensing, temperature sensing, water presence detection, and vibration sensing.

2.3. Active mode on-demand multifunctional sensing

The wireless SAW sensors can be operated in a low-power active mode to offer multiple on-demand sensing functions such as strain measurement, temperature monitoring, and detection of water presence. To demonstrate strain sensing, a wireless SAW sensor was bonded on the top surface of an aluminum cantilever beam (thickness 2 mm), and the transmitting coil was placed above the beam, as illustrated in **Figure 3a**. The distance between the transmitting coil and the wireless SAW sensor was kept constant at 20 mm. When the beam's free end was subjected to a deflection in the +*z*-direction, the SAW sensor on the beam's top surface experienced a compression strain. Hence, the spacing between adjacent electrodes decreased, further causing the sensor's S_{11}-frequency curve to shift to the right. This is confirmed by our experimental result in **Figure 3b**, showing very small valley frequency increments when the strain decreases from 0 to -0.73 mε. **Figure 3c** presents a zoomed-in view of the S_{11} curve's falling slope, confirming the S_{11} increase with the strain decrease, indicating more energy reflected by the SAW sensor at a test frequency locked on the falling slope. Using the sensing configuration illustrated in **Figure 1b**, an oscilloscope was used to measure the total signal $s_m(t)=s_t(t)+s_r(t)$, considering both the input and reflected signals. **Figure 3d** (top) shows an absolute-value waveform $|s_m(t)|$ at a locked frequency of 37.7 MHz, when the applied strain is -0.29 $m\varepsilon$. **Figure 3d** (bottom) provides a 2D view of waveform amplitude changes induced by strain changes from 0 to -0.73 $m\varepsilon$. Note that the experimental strain values are determined using the beam tip deflection and the approach in Supplementary Section S2. We also performed repeated measurements, and the statistical results are given in **Figure 3e**. These results show that the total signal's amplitude gradually decreases with the decrease of strain. This agrees with our expectation that the lower strain induces higher S_{11} and reflection signal amplitude $s_r(t)$. This higher reflection amplitude further leads to a lower amplitude of the total signal $s_m(t)$, as the input and reflected signals are out-of-phase, as characterized in **Figure S1** and explained in Section S1 of the Supporting Information.

Second, we demonstrated our fabricated SAW sensor through wireless temperature measurement. As illustrated in **Figure 4a**, a SAW sensor was placed in an oven, and a WPT transmitting coil was placed outside the oven at a distance of 25 mm away from the sensor.

When the temperature inside the oven rises, the spacing between adjacent electrodes of the SAW sensor increases due to the thermal expansion, leading to the S_{11}-frequency curve shifting to the left, as confirmed by the measurements in **Figure 4b**. Due to this curve shift, the S_{11} value gradually decreases at a test frequency of 38 MHz locked on the falling slope of the S_{11} curve (see **Figure 4c**). This indicates that the energy reflected by the SAW sensor decreases, as the temperature increases. Therefore, we expect that the amplitude of the total signal $s_m(t)$ (*i.e.*, summation of out-of-phase input and reflected signals) increases with the temperature increase. Using the sensing approach shown in **Figure 1b**, an oscilloscope was used to measure the total signal. **Figure 4d** (top) shows an absolute-value waveform $|s_m(t)|$, when the oven temperature is 70 °C. **Figure 4d** (bottom) provides a 2D view of waveform amplitude changes induced by temperature changes from 50 to 100 °C. **Figure 4e** gives a statistical analysis of waveform amplitudes acquired at different temperatures. These results reveal that the higher oven temperature results in the higher amplitude of the measure total signal. The temperature sensing experiments were performed up to 100 °C, as the silver solder used to connect different components of the sensor was not for high-temperature scenarios. To increase the temperature limit, we plan to integrate all the components directly onto the piezoelectric wafer through cleanroom fabrication.

Third, we demonstrated our fabricated wireless SAW sensor by detecting the presence of water. As illustrated in **Figure 5a**, a SAW sensor was bonded on the bottom of a Petri dish, and then deionized water was added to the Petri dish. Because water leads to energy leakage from the SAW sensor, as well as SAW velocity change,[2, 64] the wireless SAW sensor's S_{11} curve and reflected signal both change. As confirmed by the experimental results in **Figure 5b**, when the sensor is submerged in water, the S_{11} value increases, indicating more energy reflected by the SAW sensor. As the input and reflected signals are out-of-phase, a higher reflection leads to a lower total signal $s_m(t)=s_t(t)+s_r(t)$, as confirmed by the measured waveforms in **Figure 5c**.

The SAW sensor's performance parameters depend on multiple factors such as SAW speed, substrate material, and IDT design. For the SAW sensors used in our experiments, we characterized their sensitivities to different sensing parameters when the operation frequencies were around 39 MHz, the transmitter coil's input voltage was 10 V, and the coil-to-coil distance was 25 mm. For the strain sensing, the measured sensitivity was 1.7 mV/με with a tested limit of 730 με. For the temperature sensing, the measured sensitivity was 12 mV/℃ with a tested limit of 100 ℃. Although we have demonstrated the ability to monitor the changes in different conditions, these sensors are subjected to ambient fluctuations and still need improvement. To address this issue, we will leverage strategies including, but not limited to (i) introducing a protective coating or sensor housing to reduce the effects of water and humidity on temperature and strain sensors, (ii) considering temperature compensation when determining strain values, and (iii) using multiple sensors to decouple the effects of multiple parameters, such as temperature and strain.

2.4. Passive mode real-time vibration sensing

In addition to performing on-demand sensing by actively sending input signals and measuring reflected signals, we found that our wireless sensors could be operated in a power-free, passive mode for wireless vibration sensing. The mechanism of this passive sensing mode is based on the fact that the vibration of the sensor's piezoelectric substrate leads to a dynamic electric potential between the sensor's two groups of electrodes. The electric potential can further return energy to the WPT coil inductively coupled with the sensor's coil. In addition, the vibration sensing performance is affected by the distance between the inductively coupled coils. An increase in distance lowers the power transfer efficiency and reduces the signal-to-noise ratio of the measured vibration signal.

To validate this passive vibration sensing mode, we attached a sensor on a cantilever beam to measure the beam's 1st-order vibration mode, as illustrated in **Figure 6a**. Meanwhile, an

LDV was used to measure the beam vibration (see **Figure S4** for a test setup) based on the Doppler effect.[65-66] **Figure 6b** compares the raw waveforms measured by the sensor and LDV, revealing higher noise in the sensor's waveform. **Figure 6c** compares their frequency spectra obtained through the Fourier transform, both revealing a sharp resonance peak at 35 Hz. To further compare the denoised signals, we applied a frequency-domain filtering process to the acquired raw data. A band-pass filter function, shown by the green dashed line in **Figure 6c**, was used to remove the noise frequency components from the signal spectra obtained through the Fourier transform of the acquired time-domain waveforms. Then, the processed spectra with the desired frequency components were transformed back into time-domain waveforms. By comparing the denoised signals in **Figure 6d**, it can be found that the denoised signals have good agreement in terms of amplitude and phase. In addition, we changed the beam length to change its 1st-order resonance frequency, and then performed vibration measurement. The comparison in **Figure 6f** shows that our sensor can correctly measure the beam's resonance frequency at 43 Hz. The comparison in **Figure 6g** further confirms the good agreement between filtered signals measured by the wireless sensor and LDV.

3. Discussion

This paper presents wireless multifunctional SAW sensors that have been successfully demonstrated for wireless strain sensing, temperature measurement, water presence detection, and vibration sensing. To achieve these abilities, our wireless SAW sensing approach leverages a $LiNbO_3$-based SAW chip, an inductive coupling-based WPT module, and unique frequency-locked sensing mechanisms. Particularly, our approach tracks the signal's amplitude change at a frequency locked on the falling slope of a SAW sensor's S_{11}-frequency curve. Compared to previous wireless SAW sensing methods based on the measurement of resonance frequency shifts,[47-58] our approach offers multiple features. On one hand, it allows for using low-frequency (<0.1 GHz) SAW resonators for multifunctional sensing, as the effectiveness of our approach mainly depends on the sensor's quality factor (or the S_{11}-frequency curve's slope). However, existing SAW sensors are typically operated at high frequencies (*e.g.*, 0.1 to 10 GHz),[47-58] because the sensor performance highly relies on the sensor's resonance frequency. As described by Eq. (S12) in Supplementary Section S3, a small strain-induced frequency shift is nearly proportional to the sensor's resonance frequency before applying the strain. On the other hand, due to the high-frequency requirement, the widths and spacings of interdigital electrodes in previous SAW sensors are much smaller than low-frequency SAW sensors, further leading to higher manufacturing challenges such as the need for high-resolution photomasks for photolithography. Using low-frequency sensors lowers the manufacturing challenges and may allow for customized sensor fabrication through aerosol jet printing. In addition, we demonstrated the ability to wirelessly measure vibration waveforms and spectra, agreeing well with the laser vibrometry data.

Through a series of proof-of-concept experiments, we demonstrated multiple functions including sensing strain changes induced by beam bending, sensing temperature changes inside an oven, detecting water presence, as well as measuring cantilever beam vibrations. Given these successful demonstrations, more studies are needed. As this paper focuses on demonstrating the method's feasibility, the decoupling of different effects (such as strain and temperature) is not covered. Therefore, our future work will extend to the decoupling for simultaneously measuring different parameters. As revealed by the derivations in Section S3, the effects of temperature and strain on sensor outputs are different. Hence theoretically it should be possible to decouple their effects. To experimentally achieve temperature and strain decoupling, possible solutions include using an array of SAW sensors with different orientations and using two parallelly arranged SAW sensors with different substrate piezoelectric materials. Moreover, the WPT coil used in this study was manually manufactured. We plan to improve the manufacturing process by directly depositing the WPT electrodes on the SAW substrate. Additionally, we plan to increase the test temperature by using use sensor components surviving high temperatures, investigate the gas sensing ability by introducing additional materials that are sensitivity to specific gases, and explore the feasibility of further lowering the resonator's frequency.

4. Experimental Section

Design and fabrication of wireless SAW sensors

Figure S2 shows a microscopic image of a SAW sensor's interdigital electrodes and a photo of a functional wireless SAW sensor that is composed of a $LiNbO_3$ piezoelectric chip with microscale interdigital electrodes, a matching circuit, and a WPT coil. To fabricate the SAW chip with customized interdigital electrodes, we performed microfabrication in a cleanroom following the workflow illustrated in **Figure S5**. Using spin coating, a layer of photoresist (SPR3012, MicroChem, USA) is coated on a Y128-cut X-propagation $LiNbO_3$ wafer (500 µm-thick and double-side polished). Through photolithography and chemical development, the customized electrode pattern on a photomask is transferred to the $LiNbO_3$ wafer. Through e-beam evaporation, a chromium (Cr) layer with a thickness of 10 nm and a gold (Au) layer with a thickness of 90 nm are deposited on the wafer. After a lift-off process, a SAW chip with the desired IDT can be obtained. For this study, the width of the IDT's finger electrode and the spacing between adjacent electrodes are both 25.5 µm to have a SAW resonance frequency f_R around 39 MHz.

Designs of WPT coils and matching circuits

The WPT module of our wireless SAW device was designed and optimized to have a high transmission efficiency at 39 MHz. The WPT transmitting coil (inner diameter 35 mm, 4 turns) was made of a 16-gauge silicone tinned copper wire. The inductance of the transmitting coil is $L_T = 5.3$ µH at 39 MHz, measured by a vector network analyzer (E5061B, Keysight, USA). The WPT receiving coil (inner diameter 23 mm, 12 turns) was made by a winding copper wire with a diameter of 0.3 mm. This coil's inductance is $L_R = 4.8$ µH at 39 MHz. To match the WPT frequency with the SAW resonance frequency, a series-series compensation topology was used. The capacitances of matching circuits for the transmitting and receiving coils were C_T = 3.2 pF and C_R = 3.5 pF to satisfy the relation $2\pi f_R = 1/\sqrt{L_T C_T} = 1/\sqrt{L_R C_R}$.

Finite element modeling

Simulations were performed using the finite element method-based software COMSOL Multiphysics. The model (see **Figure S3** for a schematic) considers a transmitting coil with its matching circuit, a receiving coil with its matching circuit, and the surrounding air. The air domain has two regions: a thin outer layer Ω_1 with the “perfect electric conductor” condition for minimizing the boundary reflection, as well as an inner region Ω_2. Through frequency-domain simulations, we obtained both the magnetic intensity and flux fields, when a 10 V input at a frequency of 39 MHz was applied to the transmitting coil. The simulation result in a plane $\sum_1$ (illustrated **Figure S3**) was extracted and then presented in **Figure 2b**.

Laser Doppler vibrometry

The laser Doppler vibrometry was used to measure the vibration of a cantilever beam, and the measured signals were compared to signals measured by wireless SAW sensors. As illustrated by the test setup in **Figure S4**, the laser beam of an LDV (VFX-1-130, Polytec Inc.) was normal to the cantilever beam for measuring the out-of-plane displacement component of the beam vibration based on the Doppler effect. The output voltage signals from the LDV decoder were acquired by an oscilloscope (TDS 2014C, Tektronix), which also monitored the voltage signals from the WPT coil. The collected raw signals were processed using the Fourier transform to evaluate their frequency spectra and perform frequency-domain filtering.

Supporting Information

Supporting Information is available from the Wiley Online Library or from the author.

Acknowledgements

The authors acknowledge the financial support from the National Institute of General Medical Sciences of the National Institutes of Health (7R01GM144417), National Science Foundation (CMMI 2243771 and CMMI 2340016), and Nuclear Energy University Programs (DE-NE0009187). We also acknowledge the support from the Virginia Tech Advanced Research Computing Services.

Conflict of Interest

The authors declare no conflict of interest.

Data Availability Statement

The data that support the findings of this study are available from the corresponding authors upon reasonable request.

Received: ((will be filled in by the editorial staff))
Revised: ((will be filled in by the editorial staff))
Published online: ((will be filled in by the editorial staff))

References

[1] J. Friend, L. Y. Yeo, *Reviews of Modern Physics* **2011**, 83, 647.

[2] X. Ding, P. Li, S.-C. S. Lin, Z. S. Stratton, N. Nama, F. Guo, D. Slotcavage, X. Mao, J. Shi, F. Costanzo, T. J. Huang, *Lab on a Chip* **2013**, 13, 3626.

[3] Y. Q. Fu, J. K. Luo, N. T. Nguyen, A. J. Walton, A. J. Flewitt, X. T. Zu, Y. Li, G. McHale, A. Matthews, E. Iborra, H. Du, W. I. Milne, *Progress in Materials Science* **2017**, 89, 31.

[4] Q. Li, J. Liu, B. Yang, L. Lu, Z. Yi, Y. Tian, J. Liu, *IEEE Electron Device Letters* **2019**, 40, 961.

[5] J. G. Rodríguez-Madrid, G. F. Iriarte, O. A. Williams, F. Calle, *Sensors and Actuators A: Physical* **2013**, 189, 364.

[6] H. Oh, K. Lee, K. Eun, S.-H. Choa, S. S. Yang, *Journal of Micromechanics and Microengineering* **2012**, 22, 025002.

[7] F. D. Lucia, P. Z. Jr, F. Frazatto, M. Piazzetta, A. Gobbi, *Procedia Engineering* **2014**, 87, 540.

[8] X. Zhang, F. Y. Wang, L. Li, *IEEE Transactions on Ultrasonics, Ferroelectrics, and Frequency Control* **2007**, 54, 1207.

[9] J. M. Meyer, V. Schell, J. Su, S. Fichtner, E. Yarar, F. Niekiel, T. Giese, A. Kittmann, L. Thormählen, V. Lebedev, S. Moench, A. Žukauskaitė, E. Quandt, F. Lofink, in *Sensors*, Vol. 21, 2021, 8166.

[10] J. Devkota, P. R. Ohodnicki, D. W. Greve, in *Sensors*, Vol. 17, 2017, 801.

[11] A. Mujahid, A. Afzal, F. L. Dickert, in *Sensors*, Vol. 19, 2019, 4395.

[12] A. Afzal, N. Iqbal, A. Mujahid, R. Schirhagl, *Analytica Chimica Acta* **2013**, 787, 36.

[13] Z. Chen, J. Zhou, H. Tang, Y. Liu, Y. Shen, X. Yin, J. Zheng, H. Zhang, J. Wu, X. Shi, Y. Chen, Y. Fu, H. Duan, *ACS Sensors* **2020**, 5, 1657.

[14] L. Lamanna, F. Rizzi, V. R. Bhethanabotla, M. De Vittorio, *Biosensors and Bioelectronics* **2020**, 163, 112164.

[15] Y. Jiang, C. Y. Tan, S. Y. Tan, M. S. F. Wong, Y. F. Chen, L. Zhang, K. Yao, S. K. E. Gan, C. Verma, Y.-J. Tan, *Sensors and Actuators B: Chemical* **2015**, 209, 78.

[16] T. M. A. Gronewold, *Analytica Chimica Acta* **2007**, 603, 119.

[17] Y. Hur, J. Han, J. Seon, Y. E. Pak, Y. Roh, *Sensors and Actuators A: Physical* **2005**, 120, 462.

[18] W. C. Wilson, D. C. Malocha, N. Kozlovski, D. R. Gallagher, B. Fisher, J. Pavlina, N. Saldanha, D. Puccio, G. M. Atkinson, *Ieee Sensors Journal* **2009**, 9, 1546.

[19] A. Pohl, R. Steindl, L. Reindl, *Ieee Transactions on Instrumentation and Measurement* **1999**, 48, 1041.

[20] D. Mandal, S. Banerjee, in *Sensors*, Vol. 22, 2022, 820.

[21] X. Li, Q. Tan, L. Qin, X. Yan, X. Liang, in *Micromachines*, Vol. 13, 2022, 912.

[22] V. B. Raj, H. Singh, A. T. Nimal, M. U. Sharma, M. Tomar, V. Gupta, *Sensors and Actuators B: Chemical* **2017**, 238, 83.

[23] A. Mujahid, F. L. Dickert, in *Sensors*, Vol. 17, 2017, 2716.

[24] J. Devkota, P. R. Ohodnicki, D. W. Greve, *Sensors* **2017**, 17, 801.

[25] T. T. Sunil, S. Chaudhuri, V. Mishra, *Sensors and Actuators B: Chemical* **2015**, 219, 238.

[26] D. Matatagui, J. Martí, M. J. Fernández, J. L. Fontecha, J. Gutiérrez, I. Gràcia, C. Cané, M. C. Horrillo, *Sensors and Actuators B: Chemical* **2011**, 154, 199.

[27] C. Lim, W. Wang, S. Yang, K. Lee, *Sensors and Actuators B: Chemical* **2011**, 154, 9.

[28] A. J. Ricco, *The Electrochemical Society Interface* **1994**, 3, 38.

[29] B. Liu, X. Chen, H. Cai, M. Mohammad Ali, X. Tian, L. Tao, Y. Yang, T. Ren, *Journal of Semiconductors* **2016**, 37, 021001.

[30] C. Caliendo, P. Verardi, E. Verona, A. D. Amico, C. D. Natale, G. Saggio, M. Serafini, R. Paolesse, S. E. Huq, *Smart Materials and Structures* **1997**, 6, 689.

[31] A. D'Amico, E. Verona, *Sensors and Actuators* **1989**, 17, 55.

[32] X. Liang, L. Zhang, Q. Tan, W. Cheng, D. Hu, S. Li, L. Jing, J. Xiong, *Microsystems & Nanoengineering* **2023**, 9, 110.

[33] D. Silva, J. C. Mendes, A. B. Pereira, F. Gégot, L. N. Alves, in *Sensors*, Vol. 17, 2017, 1547.

[34] H. Weng, F. L. Duan, Z. Xie, S. Liu, Z. Ji, Y. Zhang, *Ieee Sensors Journal* **2020**, 20, 12679.

[35] H. Weng, F. L. Duan, Y. Zhang, M. Hu, *Ieee Sensors Journal* **2019**, 19, 11814.

[36] S. A. Zhgoon, A. S. Shvetsov, S. A. Sakharov, O. Elmazria, *IEEE Transactions on Ultrasonics, Ferroelectrics, and Frequency Control* **2018**, 65, 657.

[37] M. M. Memon, Y. Hongyuan, S. Pan, T. Wang, W. Zhang, *Journal of Electronic Materials* **2022**, 51, 5627.

[38] Z. Xu, Z. Li, *Ieee Sensors Journal* **2021**, 21, 7428.

[39] Y. Su, C. Li, M. Li, H. Li, S. Xu, L. Qian, B. Yang, *Sensors and Actuators B: Chemical* **2020**, 308, 127693.

[40] X. Le, Y. Liu, L. Peng, J. Pang, Z. Xu, C. Gao, J. Xie, *Microsystems & Nanoengineering* **2019**, 5, 36.

[41] D. Lu, Y. Zheng, A. Penirschke, R. Jakoby, *Ieee Sensors Journal* **2016**, 16, 13.

[42] Y. Tang, Z. Li, J. Ma, L. Wang, J. Yang, B. Du, Q. Yu, X. Zu, *Sensors and Actuators B: Chemical* **2015**, 215, 283.

[43] J. Schmalz, A. Kittmann, P. Durdaut, B. Spetzler, F. Faupel, M. Höft, E. Quandt, M. Gerken, in *Sensors*, Vol. 20, 2020, 3421.

[44] A. I. Mahmood, S. K. Gharghan, M. A. Eldosoky, A. M. Soliman, *IET Power Electronics* **2022**, 15, 1936.

[45] C. Zhang, J. Chen, W. Xuan, S. Huang, B. You, W. Li, L. Sun, H. Jin, X. Wang, S. Dong, J. Luo, A. J. Flewitt, Z. L. Wang, *Nature Communications* **2020**, 11, 58.

[46] X. Tan, Z. Zhou, L. Zhang, X. Wang, Z. Lin, R. Yang, J. Yang, *Nano Energy* **2020**, 78, 105307.

[47] Y. Yang, P. Mengue, H. Mishra, C. Floer, S. Hage-Ali, S. Petit-Watelot, D. Lacour, M. Hehn, T. Han, O. Elmazria, *Advanced Materials Technologies* **2022**, 7, 2100860.

[48] L. Zou, C. McLeod, M. R. Bahmanyar, *Ieee Transactions on Biomedical Engineering* **2020**, 67, 1409.

[49] O. H. Murphy, M. R. Bahmanyar, A. Borghi, C. N. McLeod, M. Navaratnarajah, M. H. Yacoub, C. Toumazou, *Biomedical Microdevices* **2013**, 15, 737.

[50] J. Devkota, D. W. Greve, T. Hong, K. J. Kim, P. R. Ohodnicki, *Ieee Sensors Journal* **2020**, 20, 9740.

[51] S. Kim, M. R. Adib, K. Lee, *Sensors and Actuators A: Physical* **2019**, 297, 111549.

[52] J. Kim, R. Luis, M. S. Smith, J. A. Figueroa, D. C. Malocha, B. H. Nam, *Sensors and Actuators A: Physical* **2015**, 224, 131.

[53] X. Dai, L. Fang, C. Zhang, H. Sun, *Journal of Sensors* **2020**, 2020, 6121907.

[54] Y. Pan, C. Yan, X. Gao, J. Yang, T. Guo, L. Zhang, W. Wang, *Microsystems & Nanoengineering* **2024**, 10, 4.

[55] Y. Fan, Y. Liu, Q. Xiao, X. Ma, X. Ji, P. Sun, *Aip Advances* **2019**, 9, 105305.

[56] A. Maskay, D. M. Hummels, M. Pereira da Cunha, *Measurement* **2018**, 126, 318.

[57] W. Luo, Q. Fu, J. Wang, Y. Wang, D. Zhou, *Ieee Sensors Journal* **2009**, 9, 1778.

[58] G. Scholl, C. Korden, E. Riha, C. C. W. Ruppel, U. Wolff, G. Riha, L. Reindl, R. Weigel, *IEEE Microwave Magazine* **2003**, 4, 68.

[59] G. Schimetta, F. Dollinger, R. Weigel, *Ieee Transactions on Microwave Theory and Techniques* **2000**, 48, 2730.

[60] C. Degen, *EURASIP Journal on Wireless Communications and Networking* **2021**, 2021, 121.

[61] A. Kurs, A. Karalis, R. Moffatt, J. D. Joannopoulos, P. Fisher, M. Soljačić, *Science* **2007**, 317, 83.

[62] M. Song, P. Jayathurathnage, E. Zanganeh, M. Krasikova, P. Smirnov, P. Belov, P. Kapitanova, C. Simovski, S. Tretyakov, A. Krasnok, *Nature Electronics* **2021**, 4, 707.

[63] V. Giurgiutiu, *Structural Health Monitoring with Piezoelectric Wafer Active Sensors*, Academic Press, Boston, MA **2008**.

[64] J. L. Rose, *Ultrasonic Waves in Solid Media*, Cambridge University Press, Cambridge **1999**.

[65] B. Cai, T. Li, L. Bo, J. Li, R. Sullivan, C. Sun, W. Huberty, Z. Tian, *Mechanical Systems and Signal Processing* **2024**, 214, 111389.

[66] Z. Tian, W. Xiao, Z. Ma, L. Yu, *Mechanical Systems and Signal Processing* **2021**, 150, 107347.

Figures

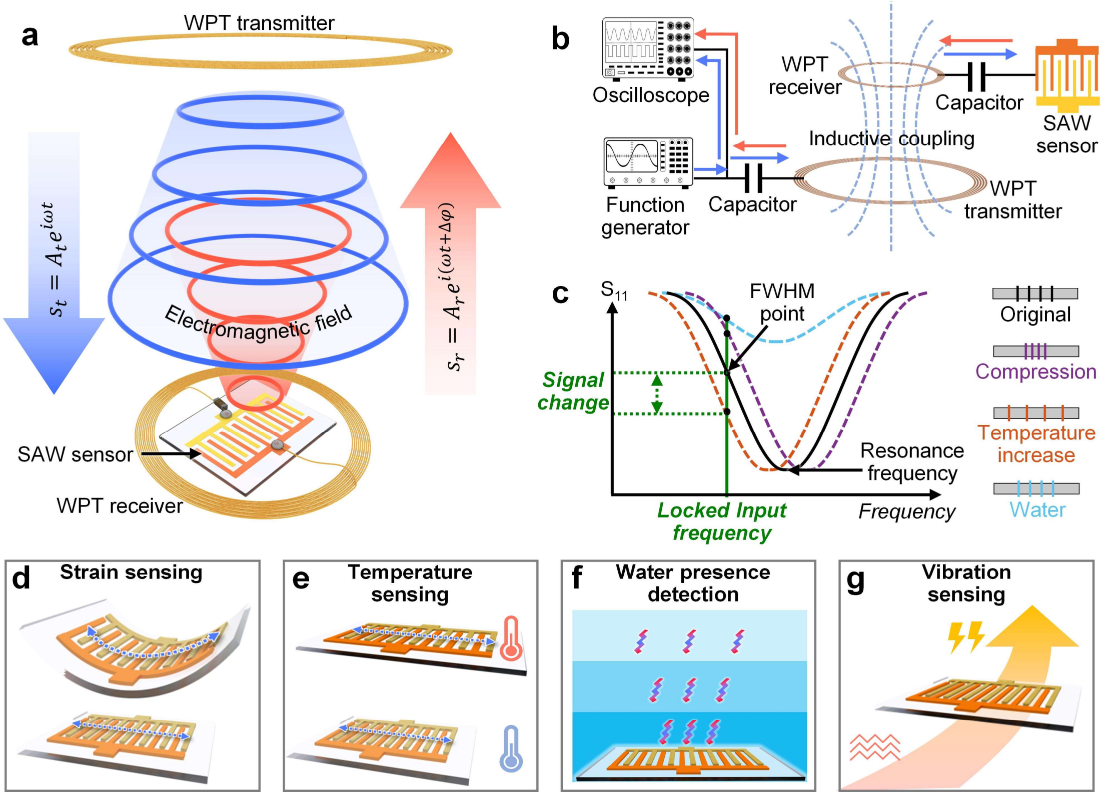

Figure 1. Mechanisms and functions of the frequency-locked wireless SAW sensors. **(a)** Schematic illustrating the mechanism of the wireless SAW sensing approach, which uses key components including a SAW chip with an IDT, a WPT transmitter with its matching circuit, and a WPT receiver with its matching circuit. **(b)** Schematic showing the sensing setup. A continuous input signal is generated by a function generator and sent to the WPT transmitter. Through inductive coupling, the input signal is wirelessly transferred to the WPT receiver and sent to the IDT in the forward direction (indicated by blue arrows). The reflected signal from the SAW sensor can return to the WPT transmitter in the reverse direction (indicated by brown arrows). An oscilloscope is used to monitor the summation of input and return signals denoted as $s_t=A_te^{i\omega t}$ and $s_r=A_re^{i(\omega t+\Delta\varphi)}$, where A_t, A_r, t, ω, and $\Delta\varphi$ are forward amplitude, return amplitude, time, angular frequency, and phase shift. (**c**) Schematic illustrating the frequency-locked sensing mechanism. At the sensor's resonance frequency, the S_{11} curve has a valley. The input signal's frequency is locked at a point on the falling slope of the S_{11}-frequency curve. When the

SAW sensor is subjected to loads (*e.g.*, uniaxial loading and bending) and environmental condition changes (*e.g.*, temperature change and water presence), the sensor's S_{11} curve experiences frequency shifts and/or value changes. Accordingly, the return signal s_r changes, and the total signal $s_m = s_t + s_r$ measured by an oscilloscope changes. The wireless SAW sensors offer multiple functions including (**d**) strain sensing, (**e**) temperature sensing, (**f**) detection of water presence, and (**g**) vibration sensing.

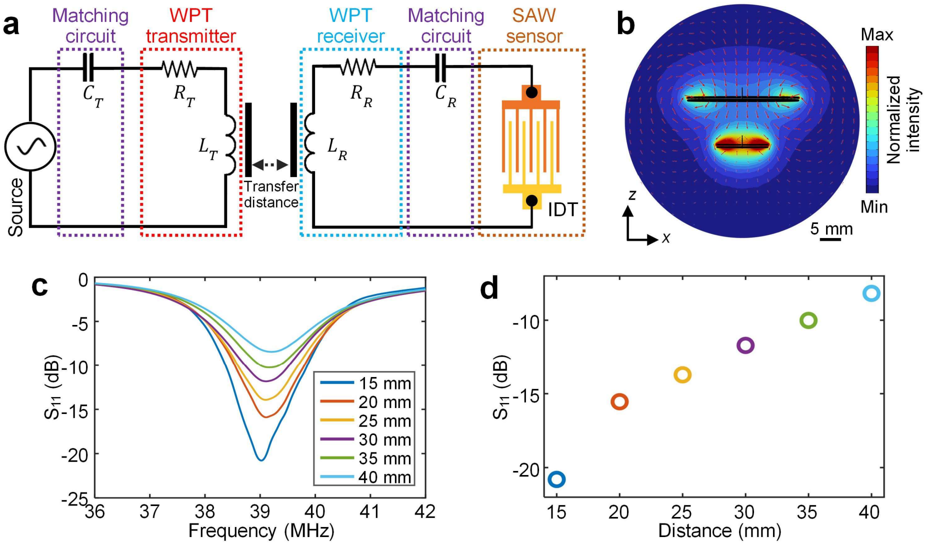

Figure 2. **Characterization of wireless SAW sensors**. **(a)** Equivalent circuit diagram of the wireless SAW sensing approach. The input side has a function generator (*i.e.*, AC power source), a matching circuit, and a WPT transmitter made of a coil inductor. The SAW sensing side has a SAW chip with an IDT resonator, a WPT receiver based on a coil inductor, and a matching circuit. The matching circuits are critical for adjusting the system parameters to enhance the power transfer efficiency. **(b)** Simulated magnetic intensity (color) and flux (arrow) fields in the *x*-*z* plane of a 3D finite element model illustrated in Figure S3. **(c)** Experimental characterization results of a sensor's S_{11}-frequency curves for cases with different transmitter-receiver distances. The results show a sharp valley at 39 MHz matching the IDT chip's SAW resonance frequency, when the transmitter-receiver distance is 15 mm. **(d)** Measured S_{11} changes at a resonance frequency of 39 MHz induced by the transmitter-receiver distance changes.

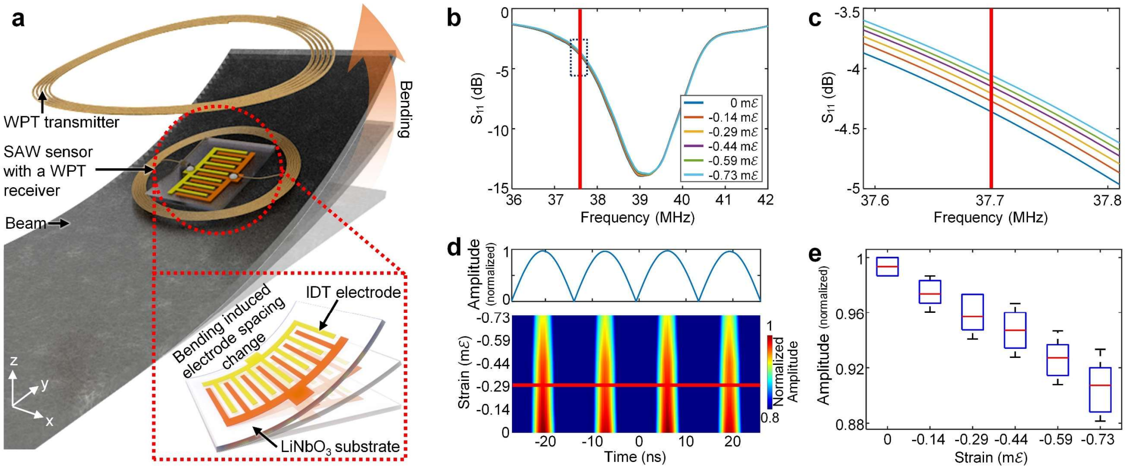

Figure 3. **Experimental results of the active mode on-demand wireless strain sensing**. **(a)** A schematic of the test setup for measuring a deflected cantilever beam's strain. When the beam tip is deflected over different distances in the +*z*-direction, the SAW sensor adhered to the beam's top surface experiences different compression strains. The applied strain induces the spacing change of the IDT electrodes, leading to changes in the S_{11}-frequency curve and the reflection signal s_r. (**b**) Experimentally measured S_{11}-frequency curves for cases with different strains on a SAW sensor. (**c**) Zoomed-in view of (**b**). (**d**, top) An absolute-value waveform $|s_m(t)|=|s_t(t)+s_r(t)|$ measured by an oscilloscope connected to the WPT transmitter at a frequency of 37.7 MHz on the falling slope of the S_{11} curve illustrated in (**b**), when the applied strain is -0.29 $m\varepsilon$. (**d**, bottom) 2D view of waveform amplitude changes induced by strain changes. (**e**) Experimentally measured waveform peak voltages for different strains. The red line within each blue box indicates the median, the bottom and top edges of each box indicate the 25th and 75th percentiles, and the whiskers extend to the extreme data points.

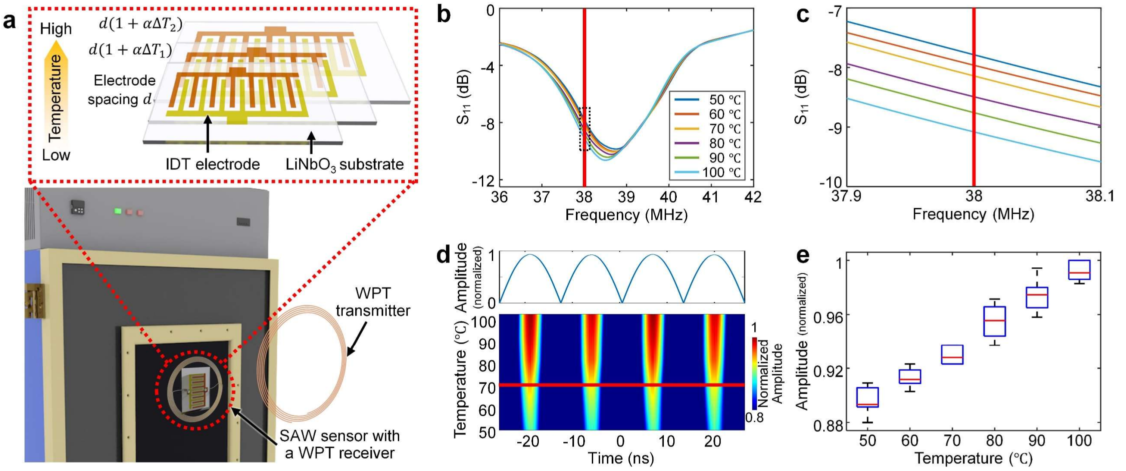

Figure 4. Experimental results of the active mode on-demand wireless temperature sensing. **(a)** A schematic of the test setup for temperature sensing using a wireless SAW sensor inside an oven. The WPT transmitter is placed outside the oven. When the oven temperature increases by ΔT, the SAW sensor undergoes thermal expansion, and the spacing d between adjacent electrodes of the IDT increases to $d(1+\alpha\Delta T)$. (**b**) Experimentally measured S_{11}-frequency curves for cases with different temperatures. With the temperature increase, both the valley frequency and S_{11} value decrease. (**c**) Zoomed-in view of (**b**). (**d**, top) An absolute-value waveform $|s_m(t)|=|s_t(t)+s_r(t)|$ measured by an oscilloscope connected to the WPT transmitter at a frequency of 38 MHz on the falling slope of the S_{11} curve illustrated in (**b**), when the oven temperature is 70 °C. (**d**, bottom) 2D view of waveform amplitude changes induced by temperature changes. (**e**) Box plot of experimentally measured waveform peak voltages at different temperatures. The red line within each blue box indicates the median, the bottom and top edges of each box indicate the 25th and 75th percentiles, and the whiskers extend to the extreme data points.

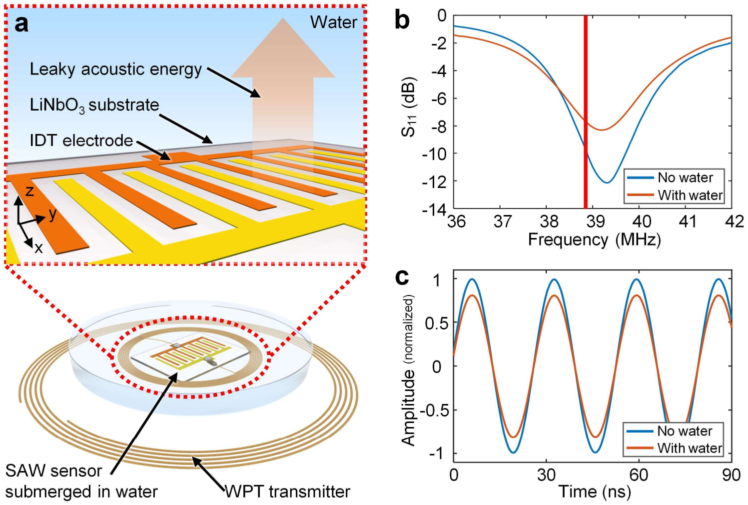

Figure 5. Experimental results of the active mode on-demand wireless detection of water presence. **(a)** A schematic of the test setup for detecting water presence using a wireless SAW sensor placed inside a Petri dish. The WPT transmitter is placed outside the dish. After submerging the wireless SAW sensor in water, the SAW energy leaks into the water, leading to changes in the S_{11}-frequency curve and the reflection signal s_r. (**b**) Experimentally measured S_{11}-frequency curves showing the S_{11} value increases after submerging the wireless SAW sensor in water. (**c**) Waveforms measured by an oscilloscope showing that signal amplitude decreases when the wireless SAW sensor is submerged in water.

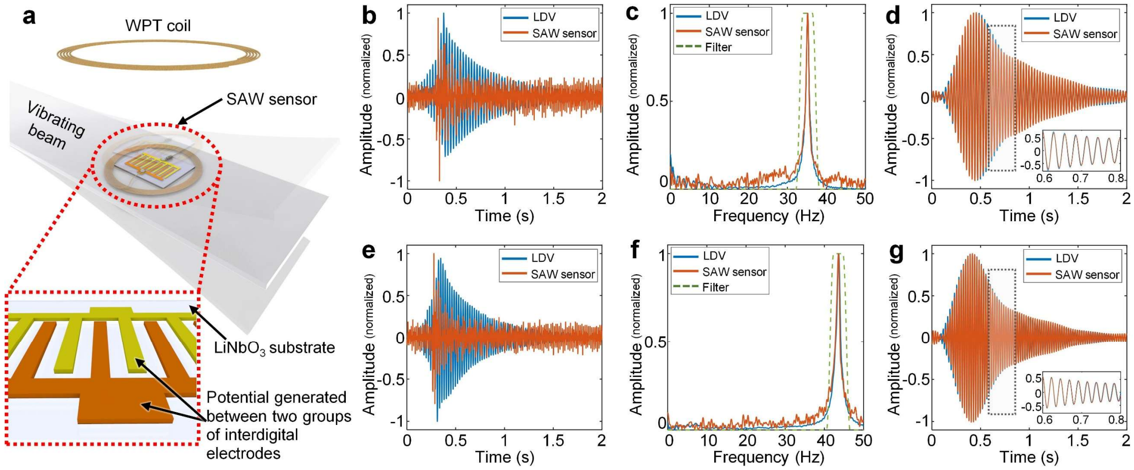

Figure 6. Experimental results of the passive mode wireless vibration measurement. **(a)** A schematic of the test setup for measuring the vibration of a cantilever beam using a wireless SAW sensor attached to the beam. When the beam is vibrating, the SAW sensor's piezoelectric substrate can convert vibration into electrical energy, leading to a dynamic potential between the two groups of interdigital electrodes of the IDT. **(b, c, d)** Acquired waveforms, frequency spectra, and filtered waveforms, respectively, when the beam's vibration frequency is 35 Hz. **(e, f, g)** Acquired waveforms, frequency spectra, and filtered waveforms, respectively, when the vibration frequency is 43 Hz. The comparison between the frequency spectra measured by an LDV and a SAW sensor shows good agreement. The filtered waveforms for the two measurement methods also agree well.